A fluid–beam model for flow in a collapsible channel

Z.X. Cai[a], X.Y. Luo[b],*

[a] Department of Mechanics, Tianjin University, Tianjin 300072, People's Republic of China
[b] Department of Mechanical Engineering, University of Sheffield, Mappin Street, Sheffield S1 3JD, UK

Abstract

This paper proposes a fluid–beam model to overcome the shortcomings of the previous fluid–membrane models on flow in collapsible channels of Luo and Pedley. The new model employs a plane strained elastic beam with large deflection and incrementally linear extension. This model gives a more realistic and general description of the problem and reduces to several simpler models including the fluid–membrane model under special parameter ranges. Both numerical and asymptotic approaches are used to study the problem. A finite element code is developed to solve the coupled nonlinear fluid–structure interactive equations simultaneously, and a moving mesh with rotating spines is used to enable a movable boundary. It is found that as the wall stiffness approaches to zero, the fluid and the beam equations at the corners where the beam joins the rigid wall are decoupled, and that asymptotic solutions exist both for the beam, and the flow which is dominated by the Stokes flow even for Reynolds number of $\mathcal{O}(10^3)$. The numerical code is validated in several different ways, and compared with the asymptotic solution at the corners. It is found that the numerical grid size has to satisfy certain conditions to resolve the boundary layers properly near the corners, especially for the smaller values of the wall stiffness. The results of the new model compare favourably with those of the fluid–membrane model for very small wall stiffness. However, different results are obtained if the wall stiffness is chosen to be applicable either to rubbers with wall thickness ratio greater than 0.01, or those of veins in the physiological range of wall thickness ratios. This model therefore provides a more realistic description to flow in collapsible channels.
© 2002 Elsevier Science Ltd. All rights reserved.

1. Introduction

Flow in collapsible tubes has a number of applications in physiological flows and medical devices and has been studied by a quite a number of researchers (Shapiro, 1977; Grotberg and Gavriely, 1989; Gavriely et al., 1989; Kamm and Pedley, 1989; Jensen and Pedley, 1989; Grotberg, 1994; Pedley and Luo, 1998; Davies and Carpenter, 1997a, b; Heil, 1997; Matsuzaki and Fujimura, 1995). In the last 20 years, modelling of flow in collapsible tubes has progressed from early "lumped-parameter" models [e.g., Bertram and Pedley (1982)], through one-dimensional models (Cancelli and Pedley, 1985; Jensen, 1990, 1992), to two-dimensional models in which the collapsible tube is represented by a channel with part of one wall replaced by a thin membrane (Lowe and Pedley, 1996; Rast 1994; Luo and Pedley, 1995, 1996, 1998, 2000; Pedley and Luo, 1998; Liang et al., 1997). Further recent progress has come through the computational work of Heil (1997), who has coupled solutions of Stokes flow to fully nonlinear three-dimensional geometrical shell theory.

The key issues of these studies have been to investigate the mechanisms of the self-excited oscillations observed in experiments (Brower and Scholten, 1975; Bertram, 1982, 1986) in which the control parameters, namely, the transmural (internal minus external) pressure and the flow rate at the upstream or downstream end, are held constant. To simulate

---

*Corresponding author. Tel: 0044 114 2227752; fax: 0044 114 2227890.
E-mail address: x.y.luo@sheffield.ac.uk (X.Y. Luo).

the self-excited oscillations requires one ultimately to extend the calculations of Heil's work (1997) to include the coupling of unsteady, three-dimensional, nonlinear Navier–Stokes equations for oscillations to arise. Such a work, however, is still a daunting computational task. Although several attempts have been made, self-excited oscillations are not yet captured (Tang et al., 1999; Tang and Yang, 2001; Scroggs et al., 2001). On the other hand, the simpler, two-dimensional simulations have successfully produced the self-excited oscillations, and shown rich dynamical behaviour of the system (Luo and Pedley, 1996, 1998, 2000).

The two-dimensional models being used in these studies, however, involve several ad hoc assumptions. First, the direction of the wall movement has to be assumed because the membrane equation alone cannot determine the movement of the material points of the elastic wall (Luo and Pedley, 1996). Secondly, the membrane model ignores the axial stiffness and hence the longitudinal stretch of the elastic wall is only balanced by a uniform tension and the transmural pressure. Thirdly, the bending stiffness of the wall is ignored. It should be noted that Liang et al. (1997) did implement the bending stiffness in their two-dimensional model. Though in their linear membrane model, the longitudinal stretch was ignored and the membrane was assumed to move vertically.

While these assumptions are reasonable for a certain range of parameters, they may lead to unrealistic results when the wall is not so thin. In addition, ignoring the longitudinal stretch can make it difficult to compare with two-dimensional experimental results [though such an experiment is extremely difficult to perform, e.g., Ikeda et al. (1998)], where the initial tension is often zero or very low.

In the present paper, a study is carried out on a new two-dimensional model in which a plane-strained elastic beam with large deflection and incrementally linear extension is used to replace the membrane. Therefore, the ad hoc assumptions mentioned above are no longer needed. The fully coupled nonlinear problem is solved using the finite element methods. To make the mesh adaptive to the moving boundary, a new spine method similar to that in Luo and Pedley (1996) is introduced which not only allows nodes to move along the spines, but also allows each spine to rotate around a fixed point. The fluid–beam model is presented in Sections 2 and 3, where some extreme cases of the new model are discussed and related with the previous models. An asymptotic analysis for the fluid–beam corners is presented in Section 4, and the moving boundary finite element methods is given in Section 5. Finally, code validations, results and the discussions are given in Sections 6, 7 and 8, respectively.

2. A fluid–beam model

2.1. The model configuration

The flow configuration is shown in Fig. 1. The rigid channel has width D, a part of the upper wall is replaced by a pre-stressed elastic beam subjected to an external pressure p_e. Steady Poiseuille flow with average velocity U_0 is assumed at the entrance. The flow is incompressible and laminar, the fluid having density ρ and viscosity μ. The beam may have large deflection but still obeys Hooke's law. The extensional and bending stiffness of the beam are EA and EJ, respectively, where E is the Young's modulus. L_u, L, and L_d are the lengths of the upstream, elastic, and downstream
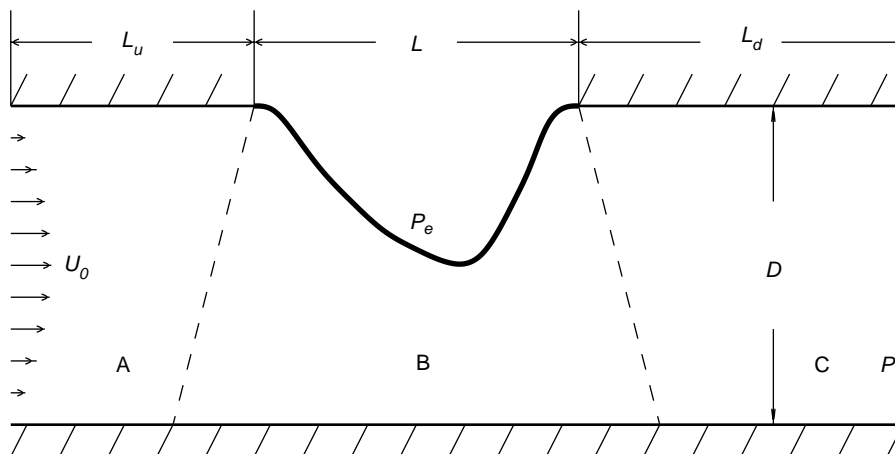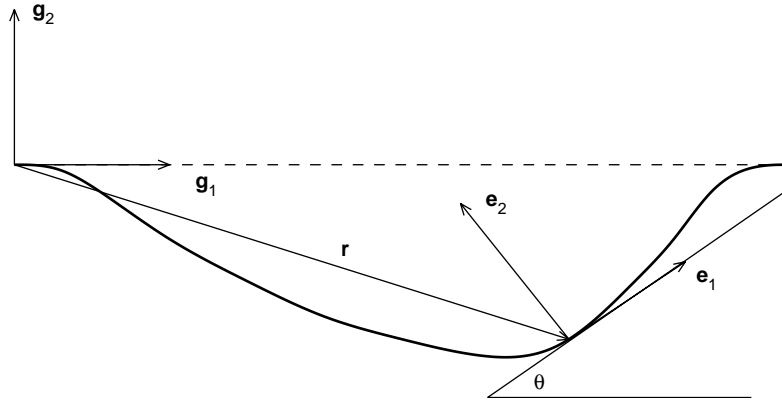

Fig. 1. The model configuration.

Fig. 2. Coordinate system for the beam.

sections, respectively. The pre-tension in the beam is T, and the density of the beam is ρ_m. Damping and rotational inertia of the beam are both neglected.

2.2. The geometry of the beam

Consider the beam as depicted in Fig. 2, where $\mathbf{g}_1$, $\mathbf{g}_2$, $\mathbf{g}_3$ are fixed reference unit vectors. Denote a typical point by $(l, 0, 0)$ in the undeformed configuration. After deformation, this point moves to

$$\mathbf{r}(l, t) = x(l, t)\mathbf{g}_1 + y(l, t)\mathbf{g}_2. \tag{1}$$

The unit vector in the deformed configuration is

$$\mathbf{e}_1 = \frac{1}{\lambda}\mathbf{r}' = \frac{1}{\lambda}(x'\mathbf{g}_1 + y'\mathbf{g}_2), \tag{2}$$

where the principal stretch of the beam is defined as

$$\lambda = \sqrt{x'^2 + y'^2}, \tag{3}$$

and the prime denotes differentiation with respect to l.

Define

$$\mathbf{e}_3 = \mathbf{g}_3, \quad \mathbf{e}_2 = \mathbf{e}_3 \times \mathbf{e}_1 = \frac{1}{\lambda}(-y'\mathbf{g}_1 + x'\mathbf{g}_2), \tag{4}$$

then $\mathbf{e}_i$ forms a moving triad. By using the formulas of Frenet [see Struik (1961) and note that the torsion vanishes for the plane curve], we obtain

$$\frac{\partial \mathbf{e}_1}{\partial l} = \lambda\kappa\mathbf{e}_2, \quad \frac{\partial \mathbf{e}_2}{\partial l} = -\lambda\kappa\mathbf{e}_1, \tag{5}$$

where the wall curvature κ is given as

$$\kappa = \frac{1}{\lambda^3}(x'y'' - y'x''). \tag{6}$$

2.3. The governing equations for the beam

Consider the motion of a differential element shown in Fig. 3. We can write the momentum equation

$$\frac{\mathrm{d}}{\mathrm{d}t}\left(\rho_m\frac{\mathrm{d}\mathbf{r}}{\mathrm{d}t}\mathrm{d}l\right) = \mathrm{d}\mathbf{F} + \mathbf{q}\mathrm{d}s, \tag{7}$$

and the angular momentum equation

$$\frac{\mathrm{d}}{\mathrm{d}t}\left(\rho_m\mathbf{r} \times \frac{\mathrm{d}\mathbf{r}}{\mathrm{d}t}\mathrm{d}l\right) = \mathrm{d}\mathbf{M} + \mathbf{r} \times \mathbf{q}\,\mathrm{d}s + (\mathbf{r} + \mathrm{d}\mathbf{r})$$
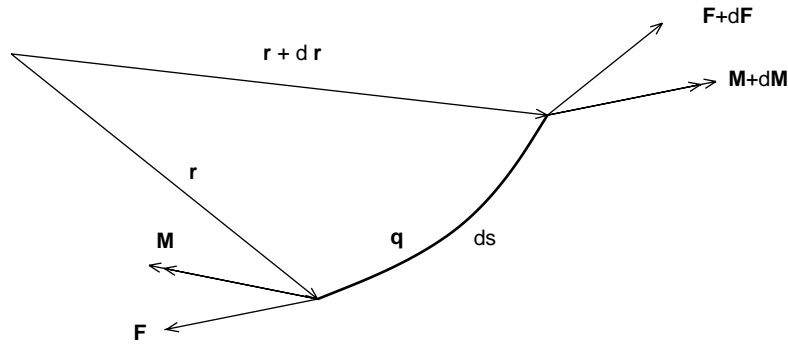$$\times (\mathbf{F} + \mathrm{d}\mathbf{F}) - \mathbf{r} \times \mathbf{F}, \tag{8}$$

Fig. 3. A differential element of the beam.

where $\mathbf{F}, \mathbf{M}$ are force and moment acting on the cross section of the beam, respectively, ρ_m is the mass density of the beam. $\mathrm{d}s$ is the length of the deformed differential element $(= \lambda \mathrm{d}l)$, and $\mathbf{q}$ is the distributive force which changes as the beam deforms.

After some straightforward manipulations and dropping the higher order terms, Eqs. (7) and (8) can be written in components:

$$\frac{\rho_m}{\lambda}\left(x'\frac{\mathrm{d}^2 x}{\mathrm{d}t^2} + y'\frac{\mathrm{d}^2 y}{\mathrm{d}t^2}\right) = F_1' - \lambda\kappa F_2 + \lambda q_1, \tag{9}$$

$$\frac{\rho_m}{\lambda}\left(-y'\frac{\mathrm{d}^2 x}{\mathrm{d}t^2} + x'\frac{\mathrm{d}^2 y}{\mathrm{d}t^2}\right) = F_2' + \lambda\kappa F_1 + \lambda q_2, \tag{10}$$

$$\lambda F_2 + M' = 0, \tag{11}$$

where variables with subscripts 1 and 2 indicate their components along $\mathbf{e}_1$ and $\mathbf{e}_2$. The other three component equations are identically satisfied.

The distributive force here is simply the fluid stresses, i.e.,

$$q_1 = \tau_n, \quad q_2 = \sigma_n - p_e, \tag{12}$$

where p_e is the external pressure, and q_2 is also called the transmural pressure. Substituting Eqs. (11) and (12) into Eqs. (9) and (10), we obtain the basic equations of motion for the beam:

$$\frac{\rho_m}{\lambda}\left(x'\frac{\mathrm{d}^2 x}{\mathrm{d}t^2} + y'\frac{\mathrm{d}^2 y}{\mathrm{d}t^2}\right) = F_1' + \kappa M' + \lambda\tau_n, \tag{13}$$

$$\frac{\rho_m}{\lambda}\left(-y'\frac{\mathrm{d}^2 x}{\mathrm{d}t^2} + x'\frac{\mathrm{d}^2 y}{\mathrm{d}t^2}\right) = -\left(\frac{1}{\lambda}M'\right)' + \lambda\kappa F_1 + \lambda\sigma_n - \lambda p_e. \tag{14}$$

Using the Kirchhoff laws for an elastic beam, the constitutive equations can be written as

$$F_1 = T + EA(\lambda - 1), \tag{15}$$

$$M = EJ(\kappa - \kappa_0), \tag{16}$$

where T is the pre-tensional axial force in the beam, κ_0 is the initial wall curvature. Substituting Eqs. (15) and (16) into Eqs. (13) and (14), we obtain the governing equations for the beam:

$$\frac{\rho_m}{\lambda}\left(x'\frac{\mathrm{d}^2 x}{\mathrm{d}t^2} + y'\frac{\mathrm{d}^2 y}{\mathrm{d}t^2}\right) = EJ\kappa\kappa' + EA\lambda' + \lambda\tau_n, \tag{17}$$

$$\frac{\rho_m}{\lambda}\left(y'\frac{\mathrm{d}^2 x}{\mathrm{d}t^2} - x'\frac{\mathrm{d}^2 y}{\mathrm{d}t^2}\right) = EJ\left(\frac{1}{\lambda}\kappa'\right)' - \lambda\kappa T - EA\lambda\kappa(\lambda - 1) - \lambda\sigma_n + \lambda p_e. \tag{18}$$

Eqs. (3), (6), (17) and (18) are the four equations required for the four unknowns x, y, λ and κ.

3. The coupled fluid–beam governing equations

3.1. The dimensionless governing equations

For convenience, we introduce the dimensionless variables (marked with an asterisk):

$$u_i^* = u_i/U_0 (i = 1, 2), \quad \sigma^* = \sigma/\rho U_0^2, \quad p^* = p/\rho U_0^2, \quad T^* = T/\rho U_0^2 D,$$

$$x^* = x/D, \quad y^* = y/D, \quad t^* = tU_0/D, \quad l^* = l/D, \quad L^* = L/D, \quad \kappa^* = \kappa D,$$

$$\rho_m^* = \rho_m/D\rho, \quad c_\lambda = EA/\rho U_0^2 D, \quad c_\kappa = EJ/\rho U_0^2 D^3, \quad \mathrm{Re} = U_0 D\rho/\mu, \tag{19}$$

where Re is the Reynolds number, while c_λ and c_κ represent the extensional and bending stiffness of the beam. It is noted that c_λ and c_κ are not independent parameters, they are related by

$$c_\lambda = 12 c_\kappa D^2/h^2, \tag{20}$$

where D is the channel height and h is the thickness of the beam.

The dimensionless governing equations for the coupled system are thus:

$$\frac{\partial u_i}{\partial t} + u_j u_{i,j} = -p_{,i} + \frac{1}{\mathrm{Re}} u_{i,jj}, \tag{21}$$

$$u_{i,i} = 0, \quad i, j = 1, 2 \tag{22}$$

$$\frac{\rho_m}{\lambda}\left(x'\frac{\mathrm{d}^2 x}{\mathrm{d}t^2} + y'\frac{\mathrm{d}^2 y}{\mathrm{d}t^2}\right) = c_\kappa \kappa \kappa' + c_\lambda \lambda' + \lambda\tau_n, \tag{23}$$

$$\frac{\rho_m}{\lambda}\left(y'\frac{\mathrm{d}^2 x}{\mathrm{d}t^2} - x'\frac{\mathrm{d}^2 y}{\mathrm{d}t^2}\right) = c_\kappa \left(\frac{1}{\lambda}\kappa'\right)' - \lambda\kappa T - c_\lambda \lambda\kappa(\lambda - 1) - \lambda\sigma_n + \lambda p_e. \tag{24}$$

Note that the asterisks have now been dropped for simplicity. Eqs. (21)–(24) involve fourth-order differentiation of x and y via Eq. (6). This makes it difficult to use the second-order finite elements employed in the existing code. To reduce the order of the equations, we introduce the angle θ (see Fig. 2) as a new independent variable, hence

$$x' = \lambda\cos\theta, \quad y' = \lambda\sin\theta, \tag{25}$$

and Eq. (3) is identically satisfied. Eq. (6) can be rewritten as

$$\theta' = \lambda\kappa. \tag{26}$$

The boundary conditions are as follows.
For the flow field:
Inlet flow ($x = 0$): $u = 6y(1 - y)$, $v = 0$;
Outflow ($x = L_u + L + L_d$): $\sigma_t = \sigma_n = 0$; (this implies a zero pressure at the downstream).

Rigid walls : $u = v = 0$ at $y = 0$, $0 \leqslant x \leqslant L_u + L + L_d$
at $y = 1$, $0 \leqslant x \leqslant L_u + L$ and $L_u + L \leqslant x \leqslant L_u + L + L_d$.

Elastic section: $u(t) = u_e(t)$; $v(t) = v_e(t)$ at $x = x_e(t)$; $y = y_e(t)$.
For the beam:
At the upstream end: $x_e = L_u, y_e = 1, \theta = 0$.
At the downstream end: $x_e = L_u + L, y_e = 1, \theta = 0$.

3.2. Special cases of the new model

Some assumptions used in the previous studies can be evaluated by considering the following special cases of the new model. This will provide some insight on how the model will behave at certain extreme situations, and what should be taken into consideration to achieve meaningful numerical results.

3.2.1. Case A: $c_\kappa \ll 1$

This is when the beam is very thin but has a moderate Young's modulus. Hence, the bending stiffness can be neglected but not the extensional stiffness. Eqs. (23) and (24) become

$$\frac{\rho_m}{\lambda}\left(x'\frac{\mathrm{d}^2 x}{\mathrm{d}t^2} + y'\frac{\mathrm{d}^2 y}{\mathrm{d}t^2}\right) = c_\lambda \lambda' + \lambda\tau_n, \tag{27}$$

$$\frac{\rho_m}{\lambda}\left(y'\frac{\mathrm{d}^2 x}{\mathrm{d}t^2} - x'\frac{\mathrm{d}^2 y}{\mathrm{d}t^2}\right) = -\lambda\kappa T - c_\lambda\lambda\kappa(\lambda - 1) - \lambda\sigma_n + \lambda p_e. \tag{28}$$

Note that in this case, there exists a boundary layer near the corners of the beam. The scale of the boundary layer is of order $\mathcal{O}(\sqrt{c_\kappa/(L^2 c_\lambda)})$ (see below), which requires very fine grids to resolve it numerically. Note that L is the dimensionless beam length with the star dropped [see Eq. (19)].

3.2.2. Case B: $\lambda \to 1$

This happens when the deformation of the beam is small and the longitudinal stretch is negligible. This could be caused either by a large value of c_λ, or a small loading. Eq. (23) only contains the higher order terms, and Eq. (24) now becomes

$$\rho_m\left(y'\frac{\mathrm{d}^2 x}{\mathrm{d}t^2} - x'\frac{\mathrm{d}^2 y}{\mathrm{d}t^2}\right) = c_\kappa\kappa'' - \kappa T - \sigma_n + p_e. \tag{29}$$

This is a commonly used model, except that vertical displacement is often assumed [e.g., Liang et al. (1997)].

3.2.3. Case C: $c_\lambda \ll 1$

Both c_κ and $c_\lambda \to 0$, and Eqs. (23) and (24) reduce to

$$\frac{\rho_m}{\lambda}\left(x'\frac{\mathrm{d}^2 x}{\mathrm{d}t^2} + y'\frac{\mathrm{d}^2 y}{\mathrm{d}t^2}\right) = \lambda\tau_n, \tag{30}$$

$$\frac{\rho_m}{\lambda}\left(y'\frac{\mathrm{d}^2 x}{\mathrm{d}t^2} - x'\frac{\mathrm{d}^2 y}{\mathrm{d}t^2}\right) = -\lambda\kappa T - \lambda\sigma_n + \lambda p_e. \tag{31}$$

If the flow is steady or the wall inertia is neglected, Eq. (31) can be rewritten as

$$-\kappa T - \sigma_n + p_e = 0. \tag{32}$$

This is the membrane equation used for steady flow by Luo and Pedley (1995). In this case, there exists a singular point at the corner if the membrane bulges out at certain angle (Moffatt, 1963), which cannot be resolved numerically (and may cause the numerical scheme to break down). An asymptotic solution for the corners in this case is derived by Lowe and Pedley (1996) for Stokes flow.

3.2.4. Case D: $c_\lambda \ll 1$ and $\lambda \to 1$

This gives $c_\kappa \to 0$, and Eq. (24) becomes

$$\rho_m\left(-y'\frac{\mathrm{d}^2 x}{\mathrm{d}t^2} + x'\frac{\mathrm{d}^2 y}{\mathrm{d}t^2}\right) - \kappa T - \sigma_n + p_e = 0. \tag{33}$$

Again, all terms in Eq. (23) are of higher order compared with those in Eq. (24); hence, they are considered to have no significant effect on the flow. Note that $[-y'(\mathrm{d}^2 x/\mathrm{d}t^2) + x'(\mathrm{d}^2 y/\mathrm{d}t^2)]$ is the acceleration along the normal direction. This is exactly the membrane equation used for unsteady flow by Luo and Pedley (1996), with the assumption that the wall only moves in the normal direction. This case implies that both the wall stiffness and the deformation of the beam are small, which is only possible for very small external forces. Such a situation is very difficult to achieve in practice. This case also has a singularity at the corners.

It is clear that although the new model is not constrained to these limits, it will exhibit the boundary layer or singularity phenomenon if the parameters fall in any of these extreme cases. This will still cause great numerical difficulty. Therefore in the following, we will study the analytical behaviour of the model near the corners.

4. The asymptotic approach

An asymptotic solution for a fluid–membrane model at the upstream corner has been studied by Lowe and Pedley (1996). In the fluid–beam model, due to the bending stiffness, such a corner singularity does not exist, hence the flow at the corner can be resolved numerically in principle. In practice, however, there still exists a small-scale boundary layer for small bending stiffness which is difficult to be resolved numerically. In order to understand the local characteristic of the flow behaviour, here we will investigate the asymptotic corner solution of the fluid–beam model for a small bending stiffness, in the similar manner as that adopted by Lowe and Pedley (1996).

4.1. Normalized equations

To simplify the analysis, we introduce the following new variables:

$$\bar{x}_i = (x_i - x_{iL})/L, \quad \bar{u}_i = u_i/L, \quad \bar{l} = l/L, \quad \bar{\kappa} = \kappa L,$$

$$\bar{T} = T/c_\lambda, \varepsilon = \frac{c_\kappa}{c_\lambda L^2}, \quad \varepsilon_1 = \frac{L}{c_\lambda \mathrm{Re}}, \quad \bar{p}_e = \frac{(p_e - p_0)L}{c_\lambda}, \quad \bar{p} = \frac{\Delta p L}{c_\lambda}, \tag{34}$$

where x_{iL} is the position of the beam end, L is the initial beam length, p_0 is a reference pressure of the fluid, and $\Delta p = p - p_0$. Using the new variables, Eqs. (21)–(26) can be written as

$$\bar{x}' = \lambda \cos \theta, \quad \bar{y}' = \lambda \sin \theta, \quad \theta' = \lambda \bar{\kappa}, \tag{35}$$

$$\varepsilon \bar{\kappa} \bar{\kappa}' + \lambda' - \lambda \varepsilon_1 \frac{\partial \bar{u}_s}{\partial n} = 0, \tag{36}$$

$$\varepsilon \left(\frac{1}{\lambda} \bar{\kappa}' \right)' - \lambda \bar{\kappa} (\bar{T} + \lambda - 1) + \lambda (\bar{p}_e - \bar{p}) = 0, \tag{37}$$

$$\varepsilon_1 \, Re \, L^2 \bar{u}_j \bar{u}_{i,j} = -\bar{p}_{,i} + \varepsilon_1 \bar{u}_{i,jj}, \quad \bar{u}_{i,i} = 0, \quad i,j = 1,2. \tag{38}$$

Note that, in Eq. (37), $\bar{p}$ is used to replace $\bar{\sigma}_n$ as they are the same on the no-slip boundary for steady flow. For a slender beam, ε is a very small constant. If Re is not too small, then ε_1 is usually also a small constant. Hence, we can denote

$$\varepsilon_1 = \varepsilon^c, \tag{39}$$

where c is a positive constant.

4.2. A closed form solution for a special case

For static fluid and zero bending stiffness ($\varepsilon = 0$), the pressure is a constant and the shear stress on the beam is zero. In this case, we can obtain a closed-form solution for Eqs. (35)–(37):

$$\lambda = \text{constant} =: \lambda_0, \quad \bar{\kappa} = \frac{\bar{p}_e}{\bar{T} + \lambda_0 - 1} =: \bar{\kappa}_0. \tag{40}$$

Integrating Eqs. (35)–(37), we have

$$\theta = \lambda_0 \bar{\kappa}_0 \bar{l} + \theta_0, \quad \bar{x} = \frac{1}{\bar{\kappa}_0} \sin \theta + \bar{x}_0,$$

$$\bar{y} = -1/\bar{\kappa}_0 \cos \theta + \bar{y}_0. \tag{41}$$

The boundary conditions are

$$\bar{x} = 0,1; \quad \bar{y} = 0,0 \quad \text{at } \bar{l} = 0,1. \tag{42}$$

Substituting Eqs. (40) and (41) into Eq. (42), we obtain

$$\theta_0 = -\lambda_0 \bar{\kappa}_0/2, \quad \bar{x}_0 = 1/2, \quad \bar{y}_0 = \frac{1}{\bar{\kappa}_0} \cos \theta_0, \tag{43}$$

where λ_0 is determined from

$$\sin \frac{\lambda_0 \bar{p}_e}{2(\bar{T} + \lambda_0 - 1)} = \frac{\bar{p}_e}{2(\bar{T} + \lambda_0 - 1)}. \tag{44}$$
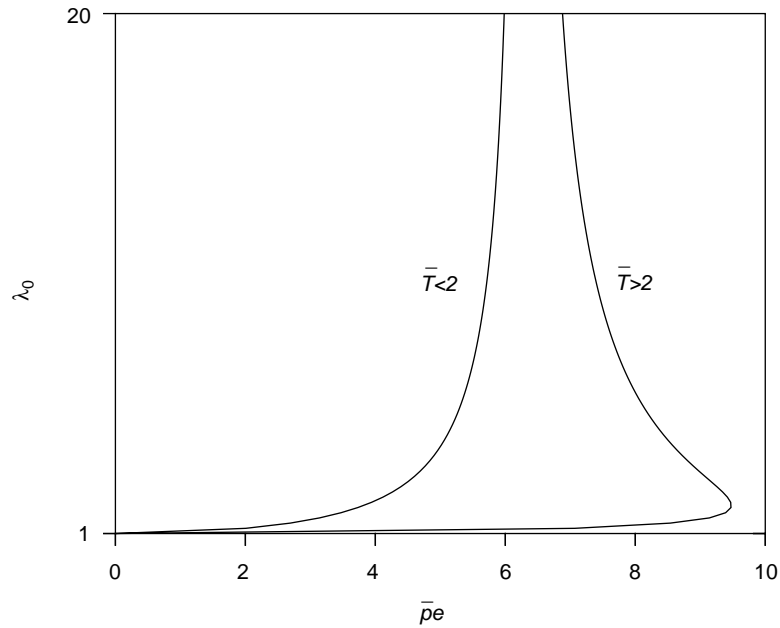
Fig. 4. The lowest branch of $\lambda_0 - \bar{p}_e$ curves for different values of $\bar{T}$.

For given values of $\bar{T}$ and $\bar{p}_e$, Eq. (44) may have multiple solutions. The physically reasonable λ_0, however, should be > 1. The lowest branch of $\lambda_0 - \bar{p}_e$ curves for different values of pre-tension $\bar{T}$ is shown in Fig. 4. It is easy to see that when $0 \leqslant \bar{T} \leqslant 2$, $\lambda_0 \to \infty$ as $\bar{p}_e \to 2\pi$. This means the beam will lose its stability at this point. Also, if $\bar{T} > 2$, the $\lambda_0 - \bar{p}_e$ curve has a bifurcation point at

$$\bar{p}_e = 2\left(\pi + \sqrt{\bar{T}^2 - 2\bar{T}} - \arccos\frac{1}{\bar{T}-1}\right), \quad \lambda_0 = \frac{(\pi - \arccos\frac{1}{\bar{T}-1})(\bar{T}-1)}{\sqrt{\bar{T}^2 - 2\bar{T}}}, \tag{45}$$

where the beam will also become unstable. To avoid these instablities, in the following, we only consider cases where $\bar{T}$ and $\bar{p}_e$ are $\mathcal{O}(1)$.

4.3. Asymptotic solutions for $\varepsilon \ll 1$

For $0 < \varepsilon \ll 1$, Eqs. (35)–(38) clearly indicate a boundary layer phenomenon. In this case, we can divide the domain into an outer region far away from the beam end where numerical solutions can be used, and an inner one where the asymptotic approach is applied, see Fig. 5.

In the inner region, we rescale Eqs. (35)–(38) by letting

$$\bar{l} = \varepsilon^\alpha \tilde{l}, \quad \theta = \tilde{\theta}, \quad \lambda = \tilde{\lambda}, \quad \kappa = \varepsilon^\beta \tilde{\kappa}, \quad \bar{x}_i = \varepsilon^\alpha \tilde{x}_i,$$

$$\bar{u}_i = \varepsilon^\gamma \tilde{u}_i, \quad \bar{p} = \varepsilon^\rho \tilde{p}, \tag{46}$$

where α is a positive constant, and variables with a tilde are $\mathcal{O}(1)$. Eqs. (35–38) can now be rewritten as

$$\varepsilon^{-\alpha}\tilde{\theta}' = \varepsilon^\beta \tilde{\lambda}\tilde{\kappa}, \tag{47}$$

$$\varepsilon^{1-\alpha+2\beta}\tilde{\kappa}\tilde{\kappa}' + \varepsilon^{-\alpha}\tilde{\lambda}' - \varepsilon^{\gamma-\alpha+c}\tilde{\lambda}\frac{\partial\tilde{u}_s}{\partial\tilde{n}} = 0, \tag{48}$$

$$\varepsilon^{1-2\alpha+\beta}\left(\frac{1}{\tilde{\lambda}}\tilde{\kappa}'\right)' - \varepsilon^\beta\tilde{\lambda}\tilde{\kappa}(\bar{T} + \tilde{\lambda} - 1) + \tilde{\lambda}\tilde{p}_e - \varepsilon^\rho\tilde{\lambda}\tilde{p} = 0, \tag{49}$$

$$\varepsilon^{2\gamma-\alpha+c}\,\mathrm{Re}\,L^2\tilde{u}_j\tilde{u}_{i,j} = -\varepsilon^{\rho-\alpha}\tilde{p}_{,i} + \varepsilon^{\gamma-2\alpha+c}\nabla^2\tilde{u}_i. \tag{50}$$
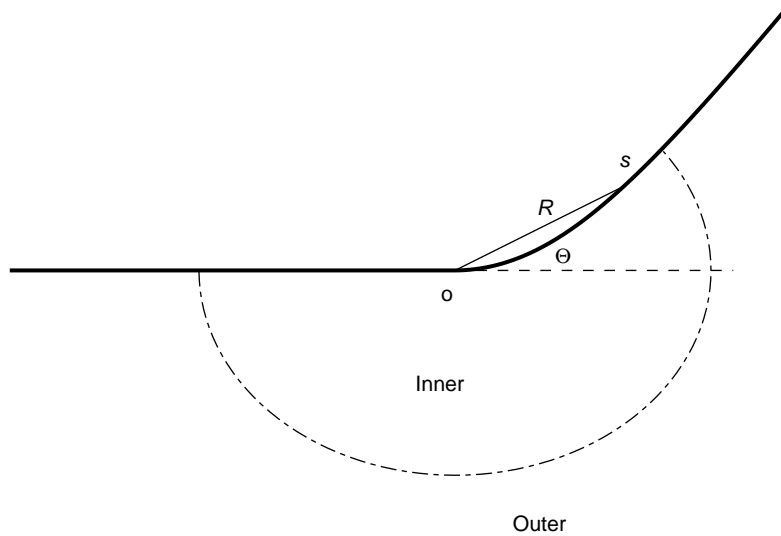
Fig. 5. The inner and outer regions of the fluid–beam corner.

On viewing Eq. (47), we immediately see that, for the leading order,

$$\beta = -\alpha. \tag{51}$$

Assume further that $\mathrm{Re}\, L^2 \ll \varepsilon^{-(\alpha+\gamma)}$, which is not too restrictive, since Re can still be of the order of thousands for the parameters we are interested in. In this case, the inertia term in Eq. (50) can be neglected, which leads to

$$\rho = \gamma + c - \alpha. \tag{52}$$

It is clear that, in the inner region, the leading order governing equations for fluid are simply Stokes equations,

$$-\tilde{p}_{,i} + \nabla^2 \tilde{u}_i = 0, \quad \tilde{u}_{i,i} = 0. \tag{53}$$

These equations can also be expressed by

$$\nabla^4 \Psi = 0, \tag{54}$$

where Ψ is the stream function.

The nature of the leading order behaviour of the beam depends on the value of $\gamma + c$, and there exhibit three possibilities.

(i) $\gamma + c < 0$: The second term in Eq. (48) is the small higher order term, so the third term is balanced by the first one which gives $\alpha = \frac{1}{2}[1 - (\gamma + c)] > \frac{1}{2}$. Eqs. (48) and (49) become

$$\tilde{\kappa}\tilde{\kappa}' - \tilde{\lambda}\frac{\partial \tilde{u}_s}{\partial \tilde{n}} = 0, \tag{55}$$

$$\left(\frac{1}{\tilde{\lambda}}\tilde{\kappa}'\right)' - \tilde{\lambda}\tilde{p} = 0. \tag{56}$$

(ii) $\gamma + c = 0$: The second term in (48) is the same order as the third one, hence $\alpha \leqslant \frac{1}{2}$, and Eqs. (48) and (49) are either

$$\tilde{\lambda}' - \tilde{\lambda}\frac{\partial \tilde{u}_s}{\partial \tilde{n}} = 0, \tag{57}$$

$$\tilde{\kappa}(\bar{T} + \tilde{\lambda} - 1) + \tilde{p} = 0 \quad \text{for } \alpha < \frac{1}{2}, \tag{58}$$

or

$$\tilde{\kappa}\tilde{\kappa}' + \tilde{\lambda}' - \tilde{\lambda}\frac{\partial \tilde{u}_s}{\partial \tilde{n}} = 0, \tag{59}$$

$$\left(\frac{1}{\tilde{\lambda}}\tilde{\kappa}'\right)' - \tilde{\lambda}\tilde{\kappa}(\bar{T} + \tilde{\lambda} - 1) - \tilde{\lambda}\tilde{p} = 0 \quad \text{for } \alpha = \frac{1}{2}. \tag{60}$$

(iii) $\gamma + c > 0$: The third term in Eq. (48) is the small higher order term, thus $\alpha = \frac{1}{2}$, and we obtain

$$\tilde{\kappa}\tilde{\kappa}' + \tilde{\lambda}' = 0, \tag{61}$$

$$\left(\frac{1}{\tilde{\lambda}}\tilde{\kappa}'\right)' - \tilde{\lambda}\tilde{\kappa}(\bar{T} + \tilde{\lambda} - 1) = 0, \tag{62}$$

$$\tilde{x}' = \tilde{\lambda}\cos\tilde{\theta}, \quad \tilde{y}' = \tilde{\lambda}\sin\tilde{\theta}, \quad \tilde{\theta}' = \tilde{\lambda}\tilde{\kappa}. \tag{63}$$

Note that the fluid and beam are decoupled in the third case. The boundary conditions for all these cases are

$$\tilde{x} = 0, \quad \tilde{y} = 0, \quad \tilde{\theta} = 0 \quad \text{at } \tilde{l} = 0, \tag{64}$$

$$\lambda \to \lambda_0, \quad \bar{\kappa} \to \bar{\kappa}_0, \quad \theta \to \theta_0 \quad \text{as } \tilde{l} \to \infty, \tag{65}$$

where λ_0, $\bar{\kappa}_0$, and θ_0 are the values of $\lambda, \bar{\kappa}, \theta$ at the interface between the inner and outer regions.

To check if any of these cases are physically feasible, we will consider the solution structure in the polar coordinate system (s, R, Θ) originated from the beam end, see Fig. 5. Note that $s \ (= \varepsilon^\alpha \tilde{s})$ is the arc-length of the beam in the deformed configuration, and $R = \varepsilon^\alpha \tilde{R}$.

The boundary conditions for the fluid are now:

$$\bar{u}_i = 0 \quad \text{at } \Theta = -\pi \text{ and } \Theta = g(R),$$
$$\bar{u}_i \to \bar{u}_{i0}, \quad \bar{p} \to \bar{p}_0 \quad \text{as } \tilde{R} \to \infty, \tag{66}$$

where $\bar{u}_{i0}, \bar{p}_0$ are the outer solutions at the interface, and $g(R)$ is an unknown function describing the shape of the beam. As $g = 0$ at $R = 0$, we can always expand $g(R)$ for $\tilde{R} \ll 1$:

$$g(R) \sim \delta R^m \quad \text{as } R \to 0, \tag{67}$$

where δ and $m \ (m > 0)$ are undetermined constants. In the similar way as Lowe and Pedley (1996), the stream function for $\tilde{R} \ll 1$ can be written as

$$\Psi = R^M f_M(\Theta), \tag{68}$$

where M is another undetermined constant, and f_M is a function of Θ and M. Substituting Eq. (68) into Eq. (54) and using the boundary conditions of $\bar{u} = \bar{v} = 0$, we find that $M = 2$ with the error of $\mathcal{O}(R^2)$ for $\bar{u}_i$. This means that $\bar{u}_i \sim R$, which gives rise to $\varepsilon^\alpha \sim \varepsilon^\gamma$, or $\gamma = \alpha \geqslant 0$ (for $R \geqslant 0$). Therefore, we know $\gamma + c$ is always positive. In other words, only case (iii) is physically possible for $\tilde{R} \ll 1$.

For $\tilde{R} \gg 1$, taking into account of Eq. (65), we can expand $g(R)$ similarly as

$$g(R) \sim \theta_0 + \delta \tilde{R}^m \quad \text{as } \tilde{R} \to \infty, \tag{69}$$

where δ and $m \ (< 0)$ are undetermined constants. The stream function for $\tilde{R} \gg 1$ can assume the same form as Eq. (68). Substituting Eq. (68) into Eq. (54) and using the boundary conditions of $\bar{u} = \bar{v} = 0$, we derive the approximate solution:

$$f_M(\Theta) = C F_1(\Theta) + D F_2(\Theta), \tag{70}$$

where C, D are undetermined constants, and F_1 and F_2 are

$$F_1(\Theta) = \sin(M - 2)\Theta - \sin M\Theta + \frac{2}{M}\cos M\pi \sin M(\Theta + \pi),$$

$$F_2(\Theta) = \cos(M - 2)\Theta - \cos M\Theta + \frac{2}{M}\sin M\pi \sin M(\Theta + \pi), \tag{71}$$

in which M depends on θ_0 via

$$\sin[(M - 1)(\theta_0 + \pi)] = -(M - 1)\sin(\theta_0 + \pi). \tag{72}$$

From Eq. (72), it is easy to see that, for $-\pi \leqslant \theta_0 \leqslant \pi/2$, M is either a complex number with a real part greater than 2, or a real number greater than 1. Since $\bar{u}_i \sim R^{M-1} \sim \varepsilon^{\alpha(M-1)} \sim \varepsilon^\gamma$, this immediately applies that $\gamma + c > 0$. Therefore, only $\gamma + c > 0$ is possible for $\tilde{R} \gg 1$.

As $\gamma + c > 0$ is true for both $\tilde{R} \ll 1$ and $\tilde{R} \gg 1$, it is reasonable to assume that only case (iii), $\gamma + c > 0$, is physically possible for the whole inner region. Thus, in the following we shall derive the asymptotic solution for this case.

4.3.1. Asymptotic solution for the beam

Since $\gamma + c > 0$, from Eqs. (46), (48) and (49), it is easy to see that in the inner region

$$\alpha = 1/2, \quad \tilde{l} \sim \varepsilon^{1/2}, \quad \bar{\kappa} \sim \varepsilon^{-1/2}. \tag{73}$$

Eq. (73) is important, as it shows that the size of the inner region is the order of $\varepsilon^{1/2}$. The curvature at the corner is the order of $\varepsilon^{-1/2}$.

Since Eqs. (61)–(63) are uncoupled to the flow inside the inner region, the beam shape near the corner is solely determined by the boundary conditions, and the influence of the flow only comes in through the interface to the outer solution.

Integration of Eq. (61) gives

$$\tilde{\lambda} + \tfrac{1}{2}\bar{\kappa}^2 = \lambda_0 + \frac{\varepsilon}{2}\bar{\kappa}_0^2. \tag{74}$$

Multiplying Eq. (62) by $\tilde{\kappa}'/\tilde{\lambda}$ and integrating the resultant equation, we obtain

$$\tilde{\kappa}'^2 = \tilde{\lambda}^2 \bar{\kappa}^2 (\bar{T} + \tilde{\lambda} - 1 + \bar{\kappa}^2/4) + c. \tag{75}$$

where c, determined by Eq. (65), is

$$c = -\varepsilon\lambda_0^2\bar{\kappa}_0^2(\bar{T} + \lambda_0 - 1 + \varepsilon\bar{\kappa}_0^2/4). \tag{76}$$

It is clear that c is an $\mathcal{O}(\varepsilon)$ constant. Hence Eq. (75) can, for the leading order, be written as

$$\tilde{\kappa}'^2 = \tilde{\theta}'^2(\bar{T} + \tilde{\lambda} - 1 + \bar{\kappa}^2/4). \tag{77}$$

Substituting Eq. (74) into Eq. (77), and dropping the $\mathcal{O}(\varepsilon)$ terms, we have

$$\tilde{\kappa}' = \pm\tilde{\theta}'\sqrt{\bar{T} + \lambda_0 - 1 - \bar{\kappa}^2/4}, \tag{78}$$

which can be integrated to give

$$\tilde{\kappa} = 2\sqrt{\bar{T} + \lambda_0 - 1}\sin(c_1 \pm \tilde{\theta}/2), \tag{79}$$

where c_1 is again determined by Eq. (65),

$$c_1 = \mp\theta_0/2. \tag{80}$$

As, near $\tilde{l} = 0$, we have $\bar{\kappa} < 0$ and $\tilde{\theta} - \theta_0 > 0$ (when $\theta_0 < 0$), Eq. (79) becomes

$$\tilde{\kappa} = -2\sqrt{\bar{T} + \lambda_0 - 1}\sin\frac{(\tilde{\theta} - \theta_0)}{2}. \tag{81}$$

The solutions of Eq. (74) and (81) can be neatly expressed using the polar coordinates:

$$\theta = \theta_0 - 4\arctan S,$$

$$\lambda = \lambda_0 + \frac{\varepsilon}{2}(\bar{\kappa}_0^2 - \bar{\kappa}^2),$$

$$\bar{\kappa} = \frac{2a\sin\frac{1}{2}\theta_0}{\cosh as + \cos\frac{1}{2}\theta_0\sinh as}, \tag{82}$$

where a is a constant, and S is a function of s defined as

$$S(s) = \tan\left(\frac{\theta_0}{4}\right)e^{-as}, \quad a = \varepsilon^{-1/2}\sqrt{\bar{T} + \lambda_0 - 1}. \tag{83}$$

From these we can recover $\bar{x}$ and $\bar{y}$ using Eq. (63).

4.3.2. Asymptotic solution for the fluid

Now, all we need to do is to find the solution for Eq. (53) or (54) under conditions (66), with $g(R)$ as a given function. The stream function can be denoted by Eq. (68) for $\tilde{R} \ll 1$ and $\tilde{R} \gg 1$. We assume that it also takes the general form of

$$\Psi = R^{M(g(R))}f_M(\Theta) \tag{84}$$

for the whole inner region; here M and $f_M(\Theta)$ are determined by

$$\sin[(M - 1)(g + \pi)] = -(M - 1)\sin(g + \pi), \tag{85}$$

$$f_M(\Theta) = A[F_1(\Theta)F_2(g) - F_2(\Theta)F_1(g)], \tag{86}$$

where A is an undetermined constant which depends on the outer solution.

Using Eq. (84), we can show that Eq. (54) is satisfied to the leading order of $\mathcal{O}(R^{M-4})$; see the appendix. The boundary conditions $\bar{u}_i = 0$ are also approximately satisfied with an error of $\mathcal{O}(R^M)$.

Denoting the pressure at the interface of the inner and outer regions by $\bar{p}_{0u}$ (upstream) and $\bar{p}_{0d}$ (downstream), we can write the pressure at the boundary as

$$
\begin{aligned}
\bar{p} &= \bar{p}_{0u} - \int_{s_u}^{s} \frac{\partial(\nabla^2 \Psi)}{\partial n} \, \mathrm{d}s \\
&= \bar{p}_{0u} - \int_{s_u}^{s} \left[\sin(\Theta - \theta) \frac{\partial(\nabla^2(R^M f_M))}{\partial R} + \cos(\Theta - \theta) \frac{\partial(\nabla^2(R^M f_M))}{R \partial \Theta} \right] \mathrm{d}s \\
&=: \bar{p}_{0u} - A P(s),
\end{aligned}
\tag{87}
$$

$$
A = \frac{\bar{p}_{0u} - \bar{p}_{0d}}{P(s_d)},
\tag{88}
$$

where s_u and s_d are, respectively, the arc length coordinates of the upstream and downstream interfaces at the boundary, and n indicates the normal direction of the boundary.

It is easy to see in Eq. (87) that p is of the order of R^{M-2}. Therefore, a singularity may occur if $M < 2$ as $R \to 0$. Interestingly, as $R \to 0$, we have $M \to 2$ and $g \to 0$. Thus we need to check the limit $\lim_{R \to 0} R^{M-2}$ carefully.

From Eq. (82), we know that $\bar{\kappa} \to 2a \sin\frac{1}{2}\theta_0$ as $R \to 0$, i.e.,

$$
\bar{x} \approx R, \quad \bar{y} \approx \tfrac{1}{2}\bar{\kappa} R^2, \quad g(R) = \arctan\left(\frac{\bar{y}}{\bar{x}}\right)
$$

$$
\approx a \sin\frac{\theta_0}{2} R \quad \text{as } R \to 0.
\tag{89}
$$

On the other hand, from Eq. (85), we have

$$
M \approx 2 - \frac{2g}{\pi} \approx 2 - \frac{2a}{\pi} \sin\frac{\theta_0}{2} R \quad \text{as } R \to 0.
\tag{90}
$$

From Eq. (90), it is easy to see that $\lim_{R \to 0} R^{M-2} = 1$. In other words, there is no singularity at the upstream corner as long as the constant a is finite. From Eq. (83), we know that this is true for $\varepsilon > 0$. Physically, this makes sense since there is no longer a sharp corner at the beam ends due to the bending stiffness of the beam. The singularity exists only when $\varepsilon \to 0$, i.e., the beam becomes a membrane, and then the curvature $\bar{\kappa}$ goes to infinity (73). It is noted, however, that when ε is not zero but very small, the curvature $\bar{\kappa}$ would undergo a rapid change from order $\varepsilon^{-1/2}$ of the inner solution to $\mathcal{O}(1)$ of the outer solution within a length range of $\mathcal{O}(\varepsilon^{1/2})$. This means that to solve the system properly using numerical methods, the grid size needs to be smaller than $\mathcal{O}(\varepsilon^{1/2})$.

5. Finite element algorithm

Since a part of the flow boundary is movable, a moving mesh is used to treat the moving boundary problem. As in Luo and Pedley (1996), the mesh is divided into three subdomains, with subdomain B located under the elastic boundary, being the movable one. In subdomain B, each node (ζ_i^k, η_i^k) is fixed to a line called spine k, which connects a fixed node (x_b^k, y_b^k) on the bottom of the domain and a node (ζ_e^k, η_e^k) attached to a material point on the beam. The spine k remains a straight line but can rotate when the beam deforms, hence all the nodes on the spines can be stretched or compressed depending on how the beam is deformed. Therefore, in the deformed mesh, the boundary nodes (ζ_e^k, η_e^k) will move to (x_e^k, y_e^k), and the internal nodes (ζ_i^k, η_i^k) will move to (x_i^k, y_i^k), see Fig. 6. The relationship between (x_i^k, y_i^k) and (x_e^k, y_e^k) is

$$
x_i^k = x_b^k + \omega_i^k (x_e^k - x_b^k),
\tag{91}
$$

$$
y_i^k = y_b^k + \omega_i^k (y_e^k - y_b^k),
\tag{92}
$$

where ω_i^k is a scale factor defined by

$$
\omega_i^k = \frac{\sqrt{(\zeta_i^k - x_b^k)^2 + (\eta_i^k - y_b^k)^2}}{\sqrt{(\zeta_e^k - x_b^k)^2 + (\eta_e^k - y_b^k)^2}}.
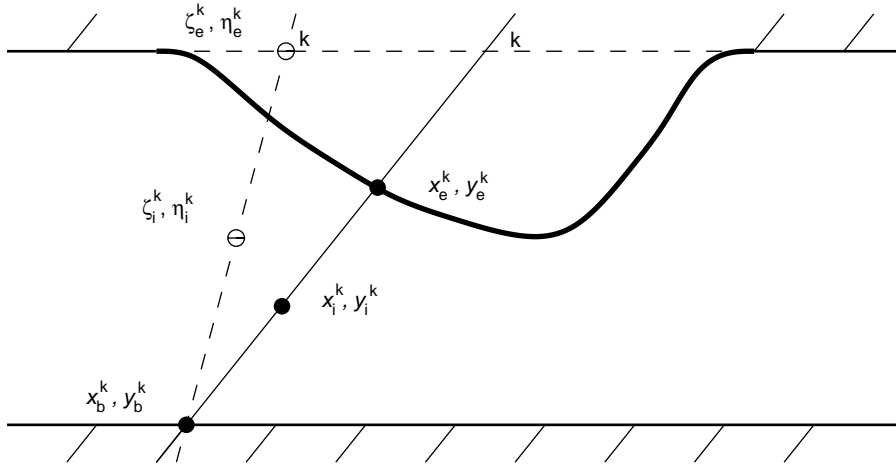\tag{93}
$$

Fig. 6. A sketch of the movable spine.

5.1. Finite element equations

Finite element equations are derived using the method of weighted residuals. The elements for flow are triangular with six nodes, and the elements for the beam are isoparameter elements with three nodes. Using the linear and quadratic shape functions L_i and N_i, we can express the discretized variables as

$$u = \sum_{i=1}^{6} u_i N_i(\zeta, \eta), \quad v = \sum_{i=1}^{6} v_i N_i(\zeta, \eta), \quad p = \sum_{i=1}^{3} p_i L_i(\zeta, \eta),$$

$$x = \sum_{i=1}^{6} x_i(x_e) N_i(\zeta, \eta), \quad y = \sum_{i=1}^{6} y_i(y_e) N_i(\zeta, \eta),$$

$$x_e = \sum_{i=1}^{3} x_{ei} N_i^*(s), \quad y_e = \sum_{i=1}^{3} y_{ei} N_i^*(s),$$

$$\theta = \sum_{i=1}^{3} \theta_i N_i^*(s), \quad \lambda = \sum_{i=1}^{3} \lambda_i N_i^*(s),$$

$$\kappa = \sum_{i=1}^{3} \kappa_i N_i^*(s); \tag{94}$$

here $N_i^*(s)$ are the values of $N_i(\zeta, \eta)$ on the elastic boundary, x_e and y_e are the values of x and y on the elastic boundary.

The Petrov–Galerkin method is used to discretize the fluid and beam equations where the weighting and shape functions are not the same. Care needs to be taken when choosing the weighting functions for the beam equations. This is due to the difficulty of making the discretized algebraic equations (23)–(26) linearly independent. To choose the appropriate weighting functions for the system, numbers of different combinations were explored, and the ones which gave converged results were implemented in the code. The one which seems to give the best performance in terms of accuracy and convergence is to choose dN_l/dl as the weighting function for the residuals (see below) R_{ex}, $R_{ey,e\theta}$, $R_{e\lambda}$, and N_l as the weighting function for $R_{e\kappa}$.

The finite element equations can be then written in a matrix form as

$$\mathbf{M} \frac{d\mathbf{U}}{dt} + \mathbf{K}(\mathbf{U})\mathbf{U} - \mathbf{F} = \mathbf{R} = 0, \tag{95}$$

where $\mathbf{U}$ is the global vector of unknowns $(u_i, v_i, p_j, x_k, y_k, \theta_k, \lambda_k, \kappa_k)$. $\mathbf{M}$ is the mass matrix, $\mathbf{K}(\mathbf{U})$ represents a nonlinear matrix including the convective and diffusion terms, $\mathbf{F}$ is the force vector, and $\mathbf{R}$ is the overall residual vector, given by

$$\mathbf{R} = (R_x, R_y, R_c, R_{ex}, R_{ey}, R_{e\theta}, R_{e\lambda}, R_{e\kappa})^{\mathrm{T}}, \tag{96}$$

where the subscripts x, y, c indicate the corresponding residuals of the x- and y-momentum and continuity in fluid, and $ex, ey, e\theta, e\lambda, e\kappa$ indicate the corresponding residuals of Eqs. (23)–(26) for the beam.

We found that, in order to get a robust numerical scheme, it is better to evaluate the integrals in the undeformed configuration, so that the variation of λ during the numerical iterations will not cause the scheme to become unstable.

It is worthwhile mentioning that, if the finite element equations of the solid are derived from the variational principles of energy as was done by Heil (1997), then this difficulty of matching the weighting and shape functions will not occur. The reason we did not choose the energy approach is because it is easier to see the physical terms in the form of Eq. (23) and (24), and to relate the model to the previous ones. This approach is also much easier to implement into the structure of the existing code.

6. Code validations and comparison with asymptotic solutions

Validations for the numerical code are performed in the following different ways. First, the fluid solver is switched off. Constant external pressure ($= 1.95$) and pre-tension ($T = 178.8$), and very small values of c_λ and c_κ ($c_\kappa = 10^{-10}$ and $c_\lambda = 10^{-5}$) are imposed. In this case, the beam behaves like a membrane, which should obey the Laplace law, $p_e = T/R$ and takes the shape of a circular arc with a radius R. As c_κ is zero in the numerical sense, we are able to impose zero bending moment ($c_\kappa\kappa = 0$) and the geometrical boundary conditions ($y = 1$) at the beam ends. The numerical results showed that, as expected, λ and κ are virtually constants along the beam, equal to 1.0001 and 0.010906, respectively, except at the close vicinity of the beam ends. Note that $R = 1/\kappa$ agrees almost exactly with that given by the Laplace law, and the numerical wall shape is indeed a circular arc.

Secondly, the fluid solver is switched on, and the numerical results for very small values of c_κ and c_λ are compared with those of the fluid–membrane model by Luo and Pedley (1996), shown in Fig. 8. It is easy to see that the difference between these two models is indeed very small.

Thirdly, for large values of c_κ and c_λ, three different combinations of shape and weighting functions were used; all of them led to the same converged results.

Finally, the numerical results at the upstream corner of the beam are compared with the analytical asymptotic solution. The agreement between the two solutions is excellent for all the four variables, see Fig. 7.

It is worth noting that in this case the assumptions made in Section 5 are indeed satisfied: $\mathrm{Re}L^2 = 7500 < < \varepsilon^{-(\alpha+\gamma)} = \varepsilon^{-M/2} \approx \varepsilon^{-1} = 2.5 \times 10^6$, and that $\varepsilon = 0.4 \times 10^{-6}$.

In carrying out the numerical calculations, the grid size is chosen such that the boundary layer of a scale $\mathcal{O}(\sqrt{c_\kappa/(L^2 c_\lambda)})$ can be resolved. In this case, the boundary layer width is estimated to be about 0.0141, and the grid is chosen to be $40 \times (60 + 120 + 240)$ with a stretch ratio of 1:10 towards the corners in both directions.
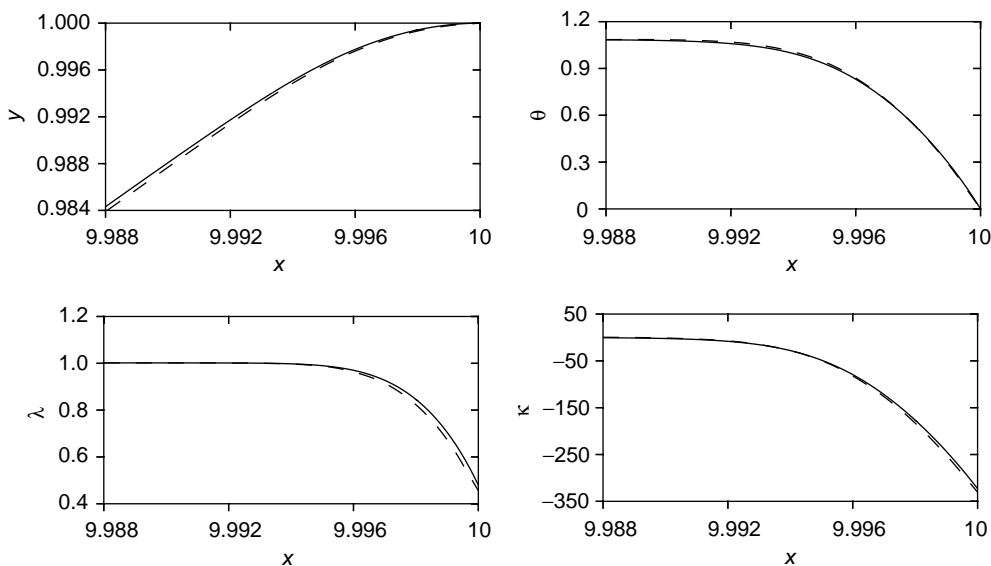

Fig. 7. Comparison between the asymptotic and numerical beam solutions at the downstream corner for $c_\lambda = 2$. Solid lines—asymptotic solutions, dotted lines—numerical solutions.

7. Results

Following Luo and Pedley (1996), the nondimensional parameters are chosen to be: $L_u = 5$, $L = 5$, $L_d = 30$, $D = 1$, Re= 300, $p_e = 1.95$, $T = 178.8/\beta$, where T is the pre-tension which can be scaled down using a constant $\beta(> 1)$. In the following, we will often use β to refer to different values of the pre-tension. The bending stiffness is in the range of $c_\kappa = 10^5 - 10^{-5}$, and a fixed ratio of $c_\kappa/c_\lambda = 10^{-5}$ is used throughout. This ratio is equivalent to choosing the thickness of the wall to be about 1% of the channel width, see Eq. (20).

The elastic wall shapes with different values of c_λ and c_κ for a fixed pre-tension ($\beta = 90$) are shown in Fig. 8. As is expected, when c_λ and c_κ are very large, the beam behaves like a rigid wall. The deformation of the wall increases as the wall stiffness decreases. The upstream end of the beam is seen to bulge out as c_λ falls below 10^2. This bulging phenomenon of the upstream end is also observed in the fluid–membrane model when the tension is below a certain value or the Reynolds number exceeds a particular value (Luo and Pedley, 1995). As c_λ becomes less than 1, the wall configuration closely resembles the one of the membrane model. In other words, the fluid–membrane model is a reasonable approximation for steady flow in collapsible channel if c_λ is of order 1 or lower.

Similarly, we can compare the results of the fluid–beam model with the fluid–membrane model for a fixed wall stiffness and with different values of pre-tension; see Fig. 9.

It can be seen that if the pre-tension of the beam is chosen to be equal to the tension in the membrane, the membrane model would present much greater wall deformation than the beam, especially in the upstream part. The wall deformation in the downstream end does not differ as much in the two models. The maximum wall collapse in the two
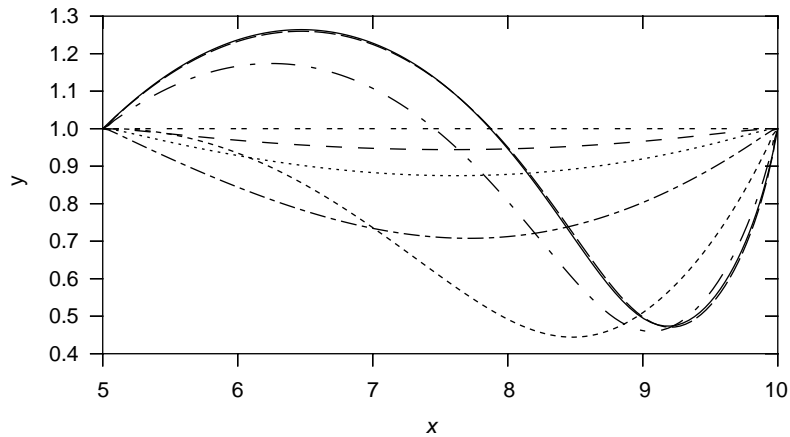

Fig. 8. The elastic wall shape at difference values of c_λ and a fixed pre-tension, $\beta = 90$: -- - -- -- , $c_\lambda = 10^{10}$; – – – – , $c_\lambda = 10^6$; .... , $c_\lambda = 10^4$; –-- --- , $c_\lambda = 1000$; --------- , $c_\lambda = 100$; —·—·— , $c_\lambda = 10$; ———— , $c_\lambda = 1$; —— , membrane. Note that the membrane shape is very close to the beam shape for $c_\lambda = 1$.
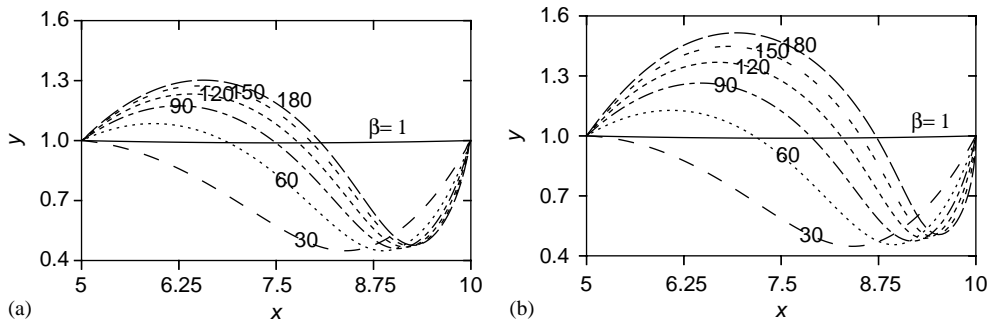

Fig. 9. The wall shapes of (a) the fluid–beam model, and (b) the fluid–membrane model (Luo and Pedley, 1996) for $c_\kappa = 10^{-4}$, $c_\lambda = 10$, and different values of the pre-tension parameter β. The pre-tension for (a) is kept to be the same as the tension for (b).
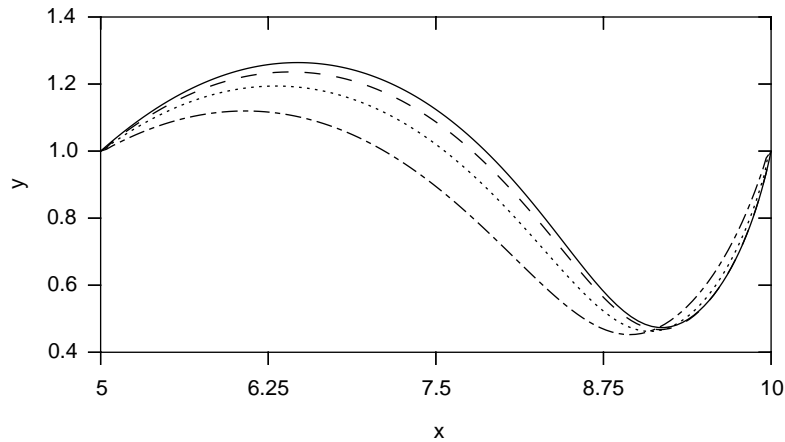
Fig. 10. The shapes of the beam for different values of c_λ. The final tension at the downstream beam end is kept to be the same as in the membrane, $\beta = 90$. $----$, $c_\lambda = 1$; .... , $c_\lambda = 10$; $-\cdot-\cdot-\cdot-$, $c_\lambda = 100$; —— , membrane.
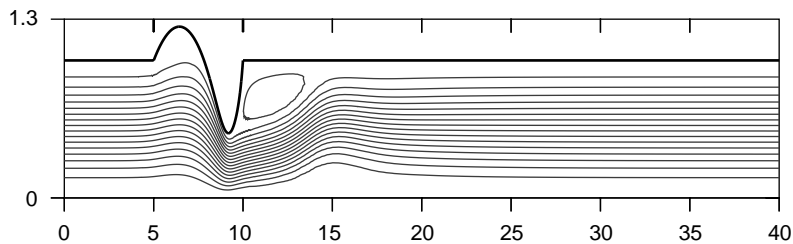

Fig. 11. Streamlines for $c_\lambda = 2$, $c_\kappa = 2 \times 10^{-5}$ and $\beta = 90$. The streamlines are plotted for an equal interval of 0.06.

cases is also comparable. However, it should be noted that the minimum y coordinate in the beam does not shift towards the downstream end as much as the membrane.

The results of the two models can also be compared while keeping the true tension at downstream end, which is the final tension after loading, of the beam to be the same as in the membrane. This then gives a different picture of the wall shapes; see Fig. 10.

In this case, the differences between the two models are not as significant as shown in Fig. 9. However, the main tendency is still that the upstream wall deformation is smaller in the beam model than in the membrane, and not surprisingly, the difference increases as the wall stiffness increases. On the other hand, the wall seems to collapse more in the beam model as the wall stiffness increases, and the minimum y location shifts towards upstream. These subtle differences may not be important for steady flow, but could have significant influences on the unsteady flow when stability of the system is considered.

The flow field for $c_\lambda = 2$, $c_\kappa = 2 \times 10^{-5}$ and $\beta = 90$ are shown as the streamlines and pressure contours in Figs. 11 and 12(a). The pressure contours at the upstream corner is shown separately in Fig. 12(b) and (c).

It is clear that the pressure singularity that existed for the fluid–membrane model at the upstream corner does not occur in the fluid–beam model. However, to resolve the boundary layer numerically, the grid has to be adjusted such that the smallest elements near the corner have dimension of about 0.002, so that the length scale of the boundary layer of $\mathcal{O}(10^{-3}L)$ can be resolved according to the asymptotic analysis. Indeed, it is found that, for smaller values of c_λ and c_κ, it is extremely difficult to obtain numerical convergence. This is because using the current mesh generator, it is not easy to decrease the grid size further without seriously distorting the elements at the corner.

Finally, results for different downstream transmural $p_e - p_d$ ($p_d = 0$) are also calculated for $\beta = 90$, and $c_\lambda = 1$; see Fig. 13(a). The corresponding wall shapes of the fluid–membrane model are shown in Fig. 13(b). It can be seen that as p_e reduces from 1 to 1.5, in both models, the elastic wall changes from the fully bulged shape into mostly collapsed shape. It looks that the effect of increasing p_e for a given tension is similar to decreasing tension for a given downstream transmural pressure. Note that, for $p_e = 3$, the solution in the fluid–membrane model is not attainable, because the
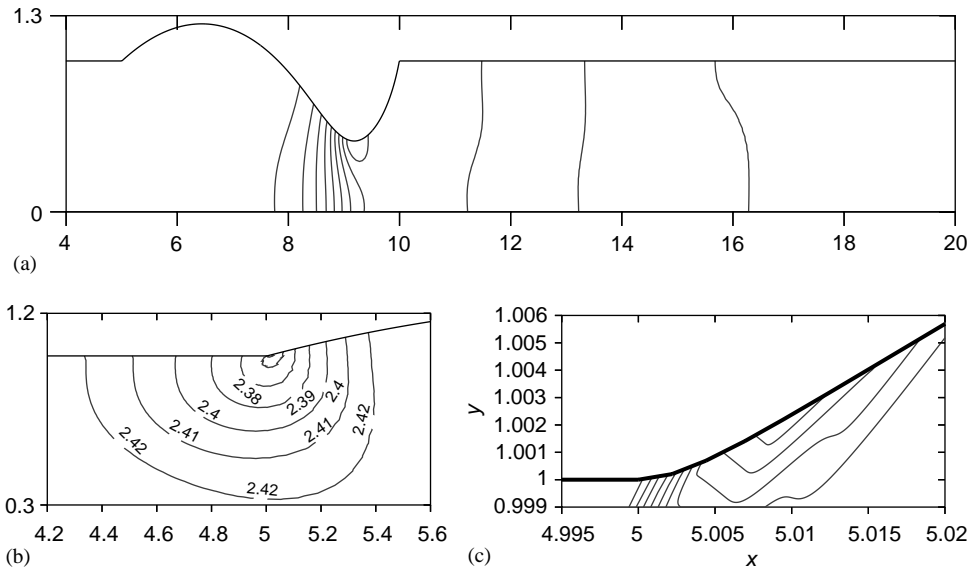
Fig. 12. Pressure contours for $c_\lambda = 2$. (a) Pressure contours in the domain from $x = 4 - 20$, with a contour interval of 0.3. (b) The contours at the upstream corner are shown in a larger scale. (c) The upstream corner is shown at an even larger scale where a smooth slope of the beam can be seen. The contour value increases from right to left from 2.354 to 2.372 with an interval of 0.002.
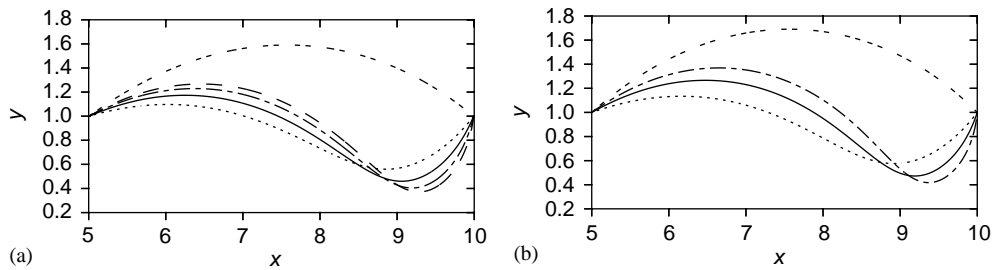

Fig. 13. The wall shapes of (a) the fluid–beam model, and (b) the fluid–membrane model (Luo and Pedley, 1996) for $c_\lambda = 1$, $\beta = 90$, and different values of p_e. The pre-tension for (a) is kept to be the same as the tension for (b). - - - - - - - -, $p_e = 1$; .... , $p_e = 1.5$; ———, $p_e = 1.95$; – - – - – - – , $p_e = 2.5$; – – – – , $p_e = 3$.

downstream membrane has the tendency of being sucked into the rigid section, which causes the numerical scheme to break down.

8. Discussion

When comparing results between the beam and membrane models for the same values of tension, we have to be careful which tension we refer to. In the beam model, the control parameter is the pre-tension, i.e., the initial tension when no fluid load is applied. The final tension in the beam varies according to the fluid loading. In the membrane model, there is no such a thing as the pre-tension. Tension is usually referred to as the one after loading, and was assumed to be a constant in the fluid–membrane model (Luo and Pedley, 1996). For small values of c_κ and c_λ, the difference between these two definitions is small, but for $c_\lambda > 1$, there are significant differences, as shown in Fig. 14, for $\beta = 90$. It is also noted that the tension in the beam model is far from being constant, especially near the downstream corner, see Fig. 15. This is because near the corner, the slope of the beam has to undergo a great change from a finite value to zero at the boundary. This causes a sudden compression in the longitudinal direction, and hence changes the final tension in the beam, since the final tension T_{final} in the beam is the sum of the pre-tension T and the change of the
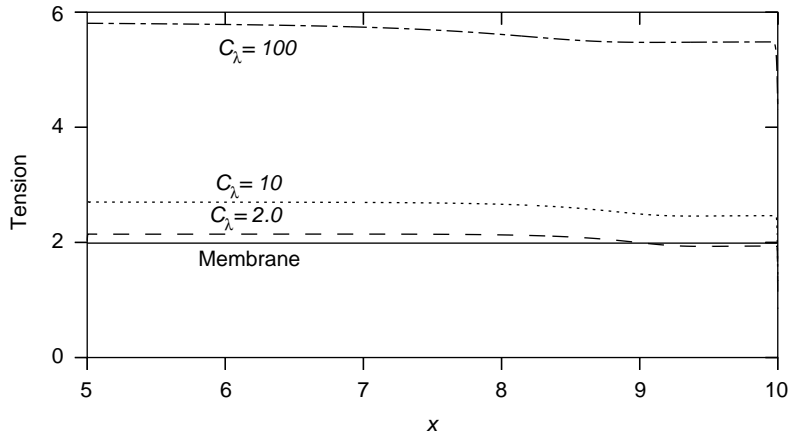
Fig. 14. Distribution of the final tension along the beam if the pre-tension is kept the same as the membrane model, with $\beta = 90$, for different values of c_λ.
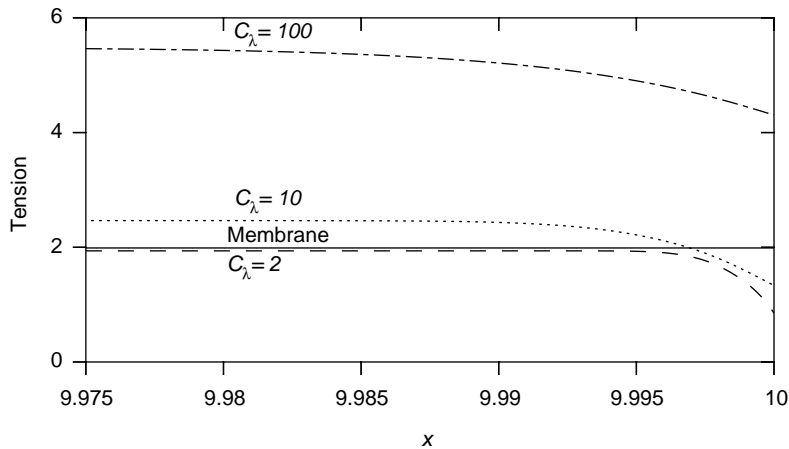

Fig. 15. The true tension of the beam at the downstream corner for different values of c_λ.

principal stretch in the longitudinal direction:

$$T_{final} = T + c_\lambda(\lambda - 1). \tag{97}$$

The upstream corner also exhibits a similar phenomenon but to a much smaller degree, as the change of wall slope is much smaller at the upstream corner.

If we keep the pre-tension in the beam to be equal to the tension in the membrane, the deformation in the membrane model is significantly greater than that in the beam model for large values of β. However, if we keep the final tension at the downstream end of the beam to be the same as the tension in the membrane, then the results of the two models do not differ so much. However, in practice, final tension cannot be used as a control parameter, since it is a calculated variable. Note that to achieve the results in Fig. 10, iterations are needed and the corresponding values of the pre-tension are found to be: $c_\lambda = 1$, $\beta = 85$, $c_\lambda = 10$, $\beta = 99$, $c_\lambda = 100$, $\beta = -71$. It is clear that, for $c_\lambda = 100$, the beam needs to be compressed to have the desired final tension. As compression is usually not applied for collapsible tube or channel experiments, this means that for larger values of the bending and stretch stiffness, there is a range of values of tension where the beam and membrane models are not comparable.

It is worth mentioning that, for the membrane model, it is found that when the tension drops below a critical value ($\beta = 180$ for Re = 300), the numerical scheme breaks down and a steady solution is not attainable (Luo and Pedley, 1995). This is also true in the beam model if c_κ falls below a certain value, although the critical value of pre-tension is
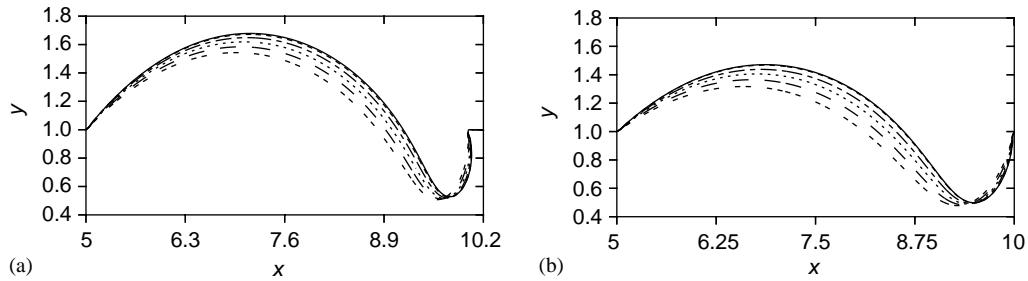
Fig. 16. The elastic wall shape at lower values of tension for the fluid–beam model: (a) $c_\lambda = 1$, the numerical scheme breaks down as $\beta > 345.3$: - - - - - - - - , $\beta = 210$; – – – – , $\beta = 240$; .... , $\beta = 270$; – - – - – - , $\beta = 300$; - - - - - - - - - , $\beta = 330$; —— , $\beta = 345.3$. (b) $c_\lambda = 10$, There is no limit for β, the wall shape approaches to a limiting shape as $\beta \to \infty$: - - - - - - - - , $\beta = 200$; – – – – , $\beta = 300$; .... , $\beta = 500$; – - – - – - , $\beta = 1000$; - - - - - - - - - , $\beta = 10^4$; —— , $\beta = 10^{10}$.
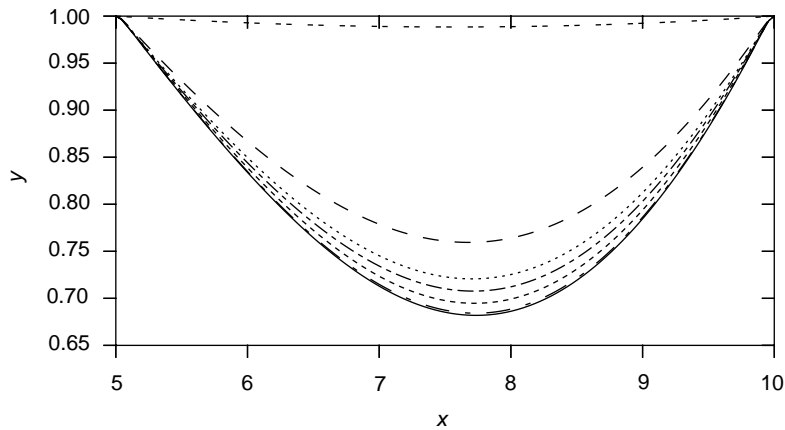

Fig. 17. The beam shapes for different values of pre-tension when $c_\lambda = 10^3$. Note that even for a zero value of tension ($\beta \to \infty$), the wall deformation is still not very large: - - - - - - - - , $\beta = 1$; – – – – , $\beta = 30$; .... , $\beta = 60$; – - – - – - , $\beta = 90$; - - - - - - - - - , $\beta = 180$; — - — - , $\beta = 1000$; —— , $\beta = 10^{10}$.

much lower in the beam model; see Fig. 16(a) for $c_\lambda = 1$. This again is because the final tension is actually much greater in the beam than the corresponding membrane.

It is found that for $c_\lambda > 3$, unlike the membrane model, there always exists a steady solution in the beam model for all values of the pre-tension, and the corresponding elastic wall approaches a limiting wall shape as $T \to 0$ ($\beta \to \infty$); see Fig. 16(b) for $c_\lambda = 10$. This is important because the value of c_λ is about 10^3–10^5 for living tissue materials,[1] and about 10^4–10^5 for rubber like material (Fung, 1993).

Fig. 17 shows the results for different values of the pre-tension T with $c_\lambda = 10^3$. It is also observed that there is no upstream bulging or downstream sucking present for $c_\lambda > 10^3$.

Even for a zero pre-tension, there still exists a steady solution as long as the bending stiffness is above a certain critical value; see Fig. 18. As mentioned before, this is the region beyond the limit of the previous membrane model. This is also in agreement with the work of Matsuzaki and Fujimura (1995), where they found that a steady solution for the channel wall always exists as long as the wall stiffness is accounted for.

Although the influence of the corner may not be important for the far field in steady flow, it could well be much more important in unsteady flow when self-excited oscillations occur. This is currently being investigated.

The limitation of the new model is that the physical linearity assumed for the beam may not be valid if the wall deformation is too large. In addition, it is still a two-dimensional approach to the original complicated three-dimensional system of flow in collapsible tubes. Therefore, the direct application of this model to collapsible tube flow is

---

[1] The value of c_λ will decrease with the wall thickness ratio. However, even in dog's venae cavae where the wall thickness ratio is lower [$h/D = 0.006$ (Pedley, 1980)], c_λ is still of $\mathcal{O}(100)$.
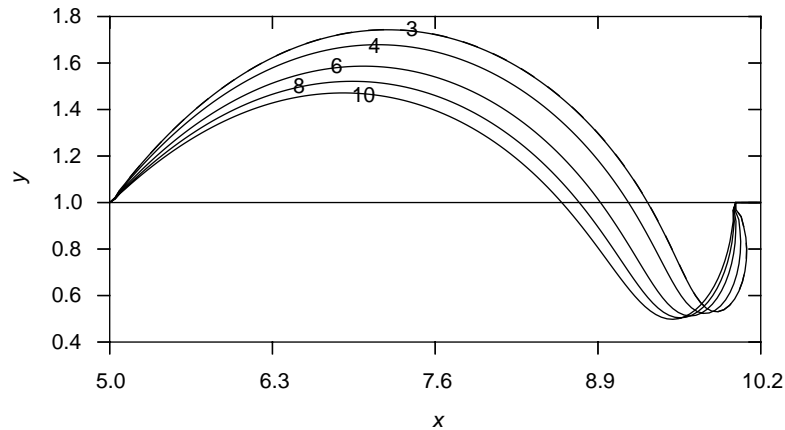
Fig. 18. The beam shapes at a zero pre-tension for different values of c_λ.

likely to be limited. Nevertheless, a study on the simpler version of the original three-dimensional fluid–structure interaction problem will serve to improve our understanding of the fundamental behaviour of the system. Most importantly, this work makes it possible to have direct comparisons with two-dimensional channel flow experiments, which can in principle be conducted. Finally, it is worth pointing out that although it is possible to apply the current numerical code to two-dimensional axisymmetric tube flow, which appears to be a step closer to the three-dimensional tube flow, it is not pursued here since we are mainly interested in the mechanisms of self-excited oscillations, which when they occur, are not axisymmetric.

9. Conclusion

A more realistic fluid–beam model for a two-dimensional flow in collapsible tubes is proposed in this paper. Both numerical and asymptotic methods are used to study this new model. A finite element code is further developed for the strongly coupled fluid–structure interaction problem, and a localized asymptotic solution is derived for the corners where a boundary layer exists. It is found that as the bending stiffness goes to zero, the curvature of the beam near the ends approaches to infinity in the manner of $\mathcal{O}(\varepsilon^{-1/2})$. Therefore to solve the problem accurately using the numerical means, it is important to have the grid size smaller than $\varepsilon^{1/2}$. It is also found that the flow and structure equations are uncoupled in the corners of the beam ends even for Re of $\mathcal{O}(10^3)$. Comparisons between the asymptotic solutions and numerical ones showed an excellent agreement.

The results of the new model are compared with the fluid–membrane model. It is discovered that for $c_\lambda \leqslant 1$, the fluid–membrane model is a very good approximation to fluid–beam model, at least for steady flow.

In the membrane model, it was found that there is a limit value of tension when a steady solution is not attainable, but for the beam model, this again depends on the wall stiffness. If the stiffness parameters are not too small, then as the pre-tension $T \to 0$, the elastic wall approaches a finite limiting shape, and there always exists a steady solution. This is because the membrane tension corresponds to the final tension in the deformed configuration, and it approximates to the pre-tension only for very small values of the wall stiffness.

For greater values of the wall stiffness, however, there are significant differences between the two models. This will be highly important for most bioengineering applications, because the wall stiffness for biological materials can be much greater than those of a membrane. Although only steady flow is considered in this paper, the model is valid for unsteady flow. Using this new model will allow us to explore the mechanisms of self-excited oscillations in a more realistic parameter region and make it possible to compare with the corresponding two-dimensional experiments.

Acknowledgements

Appendix. Error estimation for Eq. (84)

From Eqs. (85) and (86), we know that

$$f_M(\Theta) = 0, \quad \frac{\partial f_M(\Theta)}{\partial \Theta} = 0 \quad \text{at } \Theta = -\pi \text{ or } \Theta = g(R). \tag{A.1}$$

The velocities can be obtained using Eq. (84) as

$$u_R = \frac{\partial \Psi}{R \partial \Theta} = R^{M-1}\frac{\partial f_M}{\partial \Theta}, \tag{A.2}$$

$$u_\Theta = -\frac{\partial \Psi}{\partial R} = MR^{M-1}f_M + R^M\frac{\partial M}{\partial R}\left[f_M \ln R + \frac{\partial f_M}{\partial M}\right]. \tag{A.3}$$

It is easy to see that the right-hand side of Eq. (A.2) and the first term on the right-hand side of Eq. (A.3) is $\mathcal{O}(R^{M-1})$ and becomes zero at boundaries given by Eq. (A.1). Also, Eq. (86) states that f_M and $\partial f_M/\partial M$ are the same order of the constant A. Consider the fact that $R^\varepsilon \ln R \to 0$ as $R \to 0$ for any $\varepsilon > 0$, the order of the second term on the right-hand side of Eq. (A.3) depends on the order of $\partial M/\partial R$. We can estimate the order of this term from

$$\frac{\partial M}{\partial R} = \frac{\partial M}{\partial g}\frac{\partial g}{\partial \theta}\frac{\partial \theta}{\partial s}\frac{\partial s}{\partial R}, \tag{A.4}$$

where $\partial \theta/\partial s$ is the curvature of the beam, $\partial s/\partial R = 1/\cos(\theta - g)$. Using Eq. (85), we have

$$\frac{\partial M}{\partial R} = \frac{-(M-1)[\cos(g+\pi) + \cos((M-1)(g+\pi))]\, 2a \sin(\theta_0 - \theta)/2}{[\sin(g+\pi) + (g+\pi)\sin((M-1)(g+\pi))]\cos(\theta-g)}\frac{\partial g}{\partial \theta}. \tag{A.5}$$

Since $|\partial g/\partial \theta| \leqslant 1$ for the problem of concern, $\partial M/\partial R$ is roughly the same order of the constant a. This means the second term on the right-hand side of Eq. (A.3) is about $\mathcal{O}(R^M)$. So, boundary condition $u_R = 0$ is exactly satisfied, the boundary condition $u_\Theta = 0$ is approximately satisfied with the error of $\mathcal{O}(aAR^M)$.

Similarly, substituting Eq. (84) into Eq. (54), we find

$$\nabla^4\Psi = R^{M-4}\left[M^2(M-2)^2 f_M + (M^2 + (M-2)^2)\frac{\partial^2 f_M}{\partial \theta^2} + \frac{\partial^4 f_M}{\partial \theta^4}\right] + \mathcal{O}(R^{M-3}). \tag{A.6}$$

Substituting Eq. (71) and (86) into Eq. (A.6), we deduce that the first term on the right-hand side of Eq. (A.3) is zero. Hence, the errors for Eq. (54) are of $\mathcal{O}(R^{M-3})$.

References

Bertram, C.D., 1982. Two modes of instability in a thick-walled collapsible tube conveying a flow. Journal of Biomechanics 15, 223–224.

Bertram, C.D., Pedley, T.J., 1982. A mathematical model of unsteady collapsible tube behaviour. Journal of Biomechanics 15, 39–50.

Bertram, C.D., 1986. Unstable equilibrium behaviour in collapsible tubes. Journal of Biomechanics 19, 61–69.

Brower, R.W., Scholten, C., 1975. Experimental evidence on the mechanism for the instability of flow in collapsible vessels. ASME Journal of Biomechanical Engineering 13, 389–845.

Cancelli, C., Pedley, T.J., 1985. A separated-flow model for collapsible-tube oscillations. Journal of Fluid Mechanics 157, 375–404.

Davies, C., Carpenter, P.W., 1997a. Instabilities in a plane channel flow between compliant walls. Journal of Fluid Mechanics 352, 205–243.

Davies, C., Carpenter, P.W., 1997b. Numerical simulation of the evolution of Tollmien-Schlichting waves over finite compliant panels. Journal of Fluid Mechanics 335, 361–392.

Fung, Y.C., 1993. Biomechanics—Mechanical Properties of Living Tissues, 2nd Edition. Springer, New York.

Gavriely, N., Shee, T.R., Cugell, D.W., Grotberg, J.B., 1989. Flutter in flow-limited collapsible tubes: a mechanism for generation of wheezes. Journal of Applied Physiology 66, 2251–2261.

Grotberg, J.B., 1994. Pulmonary flow and transport phenonmena. Annual Review of Fluid Mechanics 26, 529–571.

Grotberg, J.B., Gavriely, N., 1989. Flutter in collapsible tubes: a theoretical model of wheezes. Journal of Applied Physiology 66, 2262–2273.

Heil, M., 1997. Stokes flow in collapsible tubes: computation and experiment. Journal of Fluid Mechanics 353, 285–312.

Ikeda, T., Heil, M., Beaugendre, H., Pedley, T.J., 1998. Experiments on flow in a two-dimensional collapsible channel. Third World Congress of Biomechanics, Abstracts, Sapporo, Japan, p. 38b.

Jensen, O.E., 1990. Instabilities of flow in a collapsed tube. Journal of Fluid Mechanics 220, 623–659.

Jensen, O.E., 1992. Chaotic oscillations in a simple collapsible tube model. ASME Journal of Biomechanical Engineering 114, 55–59.

Jensen, O.E., Pedley, T.J., 1989. The existence of steady flow in a collapsed tube. Journal of Fluid Mechanics 206, 339–374.

Kamm, R.D., Pedley, T.J., 1989. Flow in collapsible tubes: A brief review. ASME Journal of Biomechanical Engineering 111, 177–179.

Liang, S.J., Neitzel, G.P., Aidun, C.K., 1997. Finite element computations for unsteady fluid and elastic membrane interaction problems. International Journal of Numerical Methods in Fluids 24, 1091–1110.

Lowe, T.W., Pedley, T.J., 1996. Computation of Stokes flow in a channel with a collapsible segment. Journal of Fluids and Structures 9, 885–905.

Luo, X.Y., Pedley, T.J., 1995. A numerical simulation of steady flow in a 2-D collapsible channel. Journal of Fluids and Structures 9, 149–174.

Luo, X.Y., Pedley, T.J., 1996. A numerical simulation of unsteady flow in a 2-D collapsible channel. Journal of Fluid Mechanics 314, 191–225.

Luo, X.Y., Pedley, T.J., 1998. The effects of wall inertia on flow in a 2-D collapsible channel. Journal of Fluids Mechanics 363, 253–280.

Luo, X.Y., Pedley, T.J., 2000. Flow limitation and multiple solutions of flow in collapsible channel. Journal of Fluids Mechanics 420, 301–324.

Moffatt, H.K., 1963. Viscous and resistive eddies near a sharp corner. Journal of Fluid Mechanics 18, 1–18.

Matsuzaki, Y., Fujimura, K., 1995. Reexamination of steady solutions of a collapsible channel conveying fluid. A technical brief. ASME Journal of Biomechical Engineering 117, 492–494.

Pedley, T.J., 1980. The Fluid Mechanics of Large Blood Vessels. Cambridge University Press, Cambridge.

Pedley, T.J., Luo, X.Y., 1998. Modelling flow and oscillations in collapsible tubes. Theoretical and Compuational Fluid Dynamics 10, 277–294.

Rast, M.P., 1994. Simultaneous solution of the Navier–Stokes and elastic membrane equations by a finite-element method. International Journal of Numerical Methods in Fluids 19, 1115–1135.

Scroggs, R.A., Patterson, E.A., Beck, S.B.M., 2001. Numerical fluid–structure interaction model of a collapsible tube using LS-DYNA. IUTAM Symposium on Flow in Collapsible Tubes and Past other Highly Compliant Boundaries, Warwick, UK.

Shapiro, A.H., 1977. Steady flow in collapsible tubes. ASME Journal of Biomechanical Engineering 99, 126–147.

Struik, D.M., 1961. Differential Geometry, 2nd Edition. Addison-Wesley, London.

Tang, D., Yang, J., Ku, D.N., 1999. A nonlinear Axisymmetric model with fluid–wall interactions for viscous flows in stenotic elastic tubes. ASME Journal of Biomechanical Engineering 121, 494–501.

Tang, D., Yang, C. 2001. 3-D steady and unsteady blood flow in stenotic collapsible arteries with symmetric and asymmetric stenoses. Recent Advances in Biomechanics, Proceedings of First International Young Investigators Workshop on Biomechanics, Beijing, pp. 171–191.